

Co-Registration of Optoacoustic Tomography and Magnetic Resonance Imaging Data from Murine Tumour Models

Marcel Gehrung^{a,b,c,1}, Michal Tomaszewski^{a,b,1,2}, Dominick McIntyre^b,
Jonathan Disselhorst^c, Sarah Bohndiek^{a,b,*}

^a*Department of Physics, University of Cambridge, UK*

^b*Cancer Research UK Cambridge Institute, University of Cambridge, UK*

^c*Werner Siemens Imaging Center, Preclinical Imaging and Radiopharmacy, University of Tuebingen, Germany*

Abstract

As optoacoustic tomography emerges as a mainstream preclinical imaging modality, understanding the relationship between optoacoustic and other imaging biomarkers in the context of the underlying tissue biology becomes vitally important. For example, assessment of blood haemoglobin concentration and oxygenation can be achieved using OT, and also by several magnetic resonance imaging (MRI)-based techniques. To evaluate the relationship between these metrics and the relative performance of the two modalities in assessment of haemoglobin physiology, co-registration of their output imaging data is required. Unfortunately, this poses a significant challenge due to differences in the data acquisition geometries. Here, we present an integrated framework for registration of OT and MR image data in small animals. Our framework combines a novel MR animal holder, to improve animal positioning for deformable tissues, and a landmark-based software co-registration algorithm. We demonstrate that our protocol significantly improves registration of both body and tumour contours between these modalities.

*Corresponding author S E Bohndiek / Department of Physics, University of Cambridge, JJ Thomson Avenue, Cambridge, CB3 0HE, UK / Cancer Research UK Cambridge Institute, University of Cambridge, Robinson Way, Cambridge, CB2 0RE, UK / Email: seb53@cam.ac.uk

¹These authors contributed equally to this work.

²Now at: Moffitt Cancer Center, 12902 USF Magnolia Drive, Tampa, FL 33612, USA

Keywords: Optoacoustic Tomography, Magnetic Resonance Imaging, Image Registration

1. Introduction

Optoacoustic tomography (OT) is an emerging imaging modality, able to reveal the distribution of tissue optical absorption coefficient in real-time with a spatial resolution of $\sim 180 \mu\text{m}$ at $\sim 3 \text{ cm}$ penetration depth [1]. Thanks to the distinct optical absorption profiles of oxy- and deoxyhaemoglobin, acquiring OT data at multiple wavelengths (multispectral optoacoustic tomography, MSOT) makes it possible to derive optoacoustic imaging biomarkers that relate to total haemoglobin concentration (THb) and blood oxygenation (SO_2) [2]. Application of these functional MSOT imaging biomarkers has been shown to provide insight into both the architecture and function of the blood vasculature, for example, in cancer imaging, where it can be used to monitor tumour development [3, 4] and detect response to therapy [5, 6].

Functional imaging of the blood vasculature is also possible with a wide range of magnetic resonance imaging (MRI)-based techniques. Taking the example of cancer imaging, dynamic contrast enhanced (DCE) MRI [7], blood oxygen level dependent (BOLD) [8], oxygen enhanced (OE) MRI [9] and arterial spin labelling (ASL) MRI [10] have all been demonstrated to provide insight into tumour blood vessel function and the surrounding tissue hypoxia. The question thus arises, how do these different imaging techniques compare with OT and do their imaging biomarkers correlate?

The correct combination of spatial information from different imaging modalities requires careful alignment of the images and hence an efficient co-registration algorithm. This is usually achieved in both patient and small animal imaging by careful body positioning and scanning process optimisation, aided by software-based alignment. Well-established, clinically used solutions are available [11, 12] and provide excellent results for fusion of positron emission tomography (PET), computed tomography (CT) and MRI data. Unfortunately, modalities such as OT that involve different scanning geometries and positioning of the animal or patient pose a significant challenge to co-register. Successful co-registration of OT and MR images has been reported previously in the brain of small animals [13, 14], however, being contained within the skull, the brain is not subject to any deformation due to external forces, making it a relatively simple organ to co-register.

Here, we present a new integrated framework for registration of MSOT and MR image data in pre-clinical studies of small animals, which can be applied to soft, deformable tissues such as tumours. The method combines a novel animal holder design and a robust co-registration algorithm. We first describe the method and show its performance for co-localization of the internal tumour structure between the modalities. We then demonstrate the improvement in co-registration achieved by the combination of hardware and software-based solutions, compared to the manual overlay of the tumour regions with standard animal holders used for MSOT and MRI. Finally, we demonstrate the application of the co-registration framework for comparison of perfusion-based data recorded using MSOT and MRI.

2. Methods

2.1. Animal Experiments

All animal procedures were conducted in accordance with project (70-8214) and personal license (IDCC385D3) issued under the United Kingdom Animals (Scientific Procedures) Act, 1986 and were approved locally under compliance form number CFSB0671. Subcutaneous tumours were established in male BALB/c nude mice (Charles River, 7-10 weeks old, 17-22g) by inoculation of cells from one of three different cancer cell lines in both flanks (1.5×10^6 LNCaP prostate adenocarcinoma cells, $n=3$ mice; 1.5×10^6 PC3 prostate adenocarcinoma cells, $n=3$ mice; 1×10^6 mouse K8484 pancreatic adenocarcinoma cells, $n=3$ mice) in $100 \mu\text{L}$ phosphate buffered saline (PBS). Using three different cell lines allowed us to investigate the co-registration procedure across a range of morphological and functional characteristics.

2.2. Multispectral Optoacoustic Tomography (MSOT)

An MSOT inVision 256-TF commercial small animal imaging system (iThera Medical GmbH) was used. Briefly, a tunable optical parametric oscillator (OPO) pumped by an Nd:YAG laser provides excitation pulses with a duration of 9 ns at wavelengths from 660 nm to 1200 nm at a repetition rate of 10 Hz with a wavelength tuning speed of 10 ms and a peak pulse energy of 90 mJ at 720 nm. Ten arms of a fibre bundle provide uniform illumination of a ring-shaped light strip of approximately 8 mm width. For ultrasound detection, 256 toroidally focused ultrasound transducers with a centre frequency of 5 MHz (60% bandwidth) are organized in a concave array of 270 degree angular coverage and a radius of curvature of 4 cm.

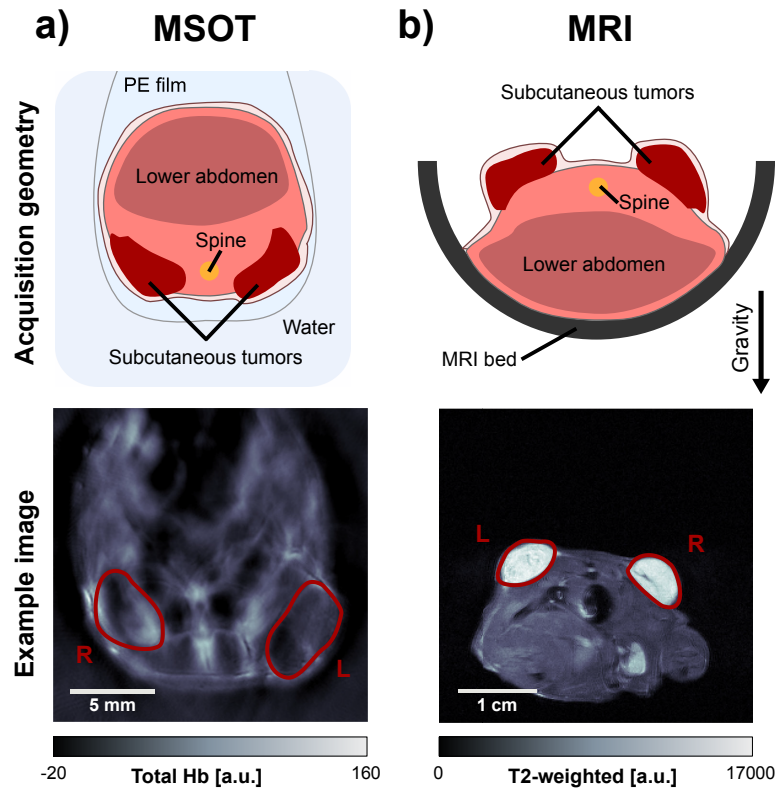


Figure 1: **Conventional MSOT and MRI holder geometries.** (a) Animal holder geometry and example image showing the total haemoglobin signal after spectral unmixing, acquired using MSOT. (b) Conventional animal holder geometry and example fast spin-echo image from MRI.

69 Mice were prepared according to our standard operating procedure [15].
70 Each mouse was anaesthetised using <3% isoflurane and moved into a custom
71 animal holder (iThera Medical GmbH), wrapped in a thin polyethylene
72 membrane, with ultrasound gel (Aquasonic Clear, Parker Labs) used to
73 couple the skin to the membrane. The holder was then placed within the
74 MSOT system and immersed in degassed water maintained at 36 °C. The
75 mouse was allowed to stabilise for 15 minutes within the system prior to
76 initialisation of the scan and its respiratory rate was then maintained in the
77 range 70-80 bpm with ~1.8% isoflurane concentration for the entire scan.
78 The imaging slice was chosen to show largest cross-sectional area of the

79 tumours on one or both flanks where possible. Images were acquired in the
80 single slice using 10 wavelengths between 700 nm and 880 nm and averaging
81 of signals from 6 pulses per wavelength; a single slice acquisition was 5.5s in
82 duration. For Oxygen Enhanced Optoacoustic Tomography, 70 such images
83 were acquired continuously, with the breathing gas switched from medical air
84 (21% Oxygen) to pure oxygen (100% Oxygen) after 30 scans, for the purpose
85 of quantification of the response in blood oxygen saturation to such defined
86 oxygen challenge.

87 *2.3. Magnetic Resonance Imaging (MRI)*

88 A 9.4 T Agilent MRI system (Agilent, Santa Clara, USA) running VnmrJ
89 3.1, using an Agilent quadrature transmit/receive millipede volume coil
90 of 38 mm inner diameter was used. The same anaesthesia protocol as for
91 optoacoustic imaging experiments was maintained. A physiological monitoring
92 system was used for observing mouse status and for sequence triggering (SAII,
93 Stony Brook, NY, USA). The core temperature of the mouse was monitored
94 using a rectal probe, and stabilized to 37 °C using an air heating system.
95 Axial multislice T2-weighted images were acquired covering the entire tumour
96 using a respiratory-gated fast spin-echo sequence (field of view 40mm, slice
97 thickness/gap 0.95/0.05mm, TR 2000ms, echo spacing 9ms, echo train length
98 8, effective TE 36ms, 2 averages, 3-4 slices acquired per gate) with chemical-
99 shift-selective fat suppression.

100 Dynamic contrast enhanced (DCE)-MRI data were acquired using a spoiled
101 gradient echo sequence (field of view 40mm, 2mm slice, 128x128 points, TR
102 20ms, TE 1.62ms, 2 averages). 10 images were acquired during the 1 minute
103 prior to administration of contrast agent (Gadavist, Bayer, 200µmol/kg) to
104 provide a baseline reference and 120 images were acquired in the 11 minutes
105 after injection.

106 *2.4. Hardware Co-registration*

107 To facilitate co-registration of MSOT and MRI data, a new small animal
108 holder was developed to reproduce the spatial positioning and body deformation
109 of the MSOT (Figure 1a) during the MRI acquisition as accurately as
110 possible. This was achieved using a silicone bed (Figure 2a), fabricated based
111 on photogrammetry of a mouse suspended in PE film, performed with the
112 software 3DF Zephyr v3.5 (3DFLOW, Italy). The deformation in the resulting
113 3D model was transferred to an isosurface extraction from the Digimouse
114 atlas and subsequently converted into a 3D model (Figure 2b). The resulting

115 model was converted into a negative mold in STL file format, then printed
 116 with Polylactic acid (PLA) using an Anet A6 3D printer (Anet, China),
 117 instructed with the slicer software Ultimaker Cura 2.6. The 3D printed mold
 118 was inserted into a conventional MRI bed and the resulting cavity was filled
 119 with silicone (Polycraft T15 Translucent Silicone, MB Fibreglass) before being
 120 cured for 24 hours. Subsequently, the negative mold was removed, the silicone
 121 bed taken out and the excess silicone trimmed.

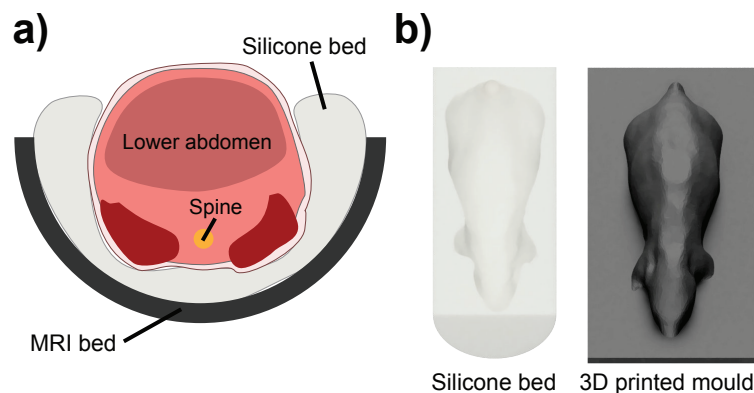


Figure 2: **Novel MRI holder geometry.** (a) Design of the silicone holder to achieve a comparable anatomical cross-section within MRI and MSOT. (b) Rendering of the silicone bed and the corresponding 3D printed mold.

122 After imaging in the MSOT, mice were maintained under anaesthesia and
 123 transferred for MRI. A subset of $n=4$ mice (3 LNCaP tumour bearing and
 124 1 PC3 tumour bearing) underwent MRI placed in the prone position in a
 125 half-pipe plastic holder, with the tumours on the back facing upwards using
 126 the conventional MRI holder geometry (Figure 1 b).

127 The remaining 5 animals (2 PC3 tumour bearing and 3 K8484 tumour
 128 bearing) were scanned in the custom silicone holder (Figure 1 c,d). Transfer
 129 into the silicone MRI bed was made in a smooth motion while maintaining
 130 the supine orientation of the mouse to preserve the positioning. The silicone
 131 bed showed a large, broad nuclear magnetic resonance excitation at 7ppm
 132 upfield of water, which was clearly visible in fast spin-echo images. Image
 133 registration was greatly simplified by suppressing this signal, as the silicone
 134 is not present in the MSOT image data. Therefore, for imaging sessions
 135 employing the silicone bed, a modified chemical-shift selective fat suppression
 136 sequence was employed, using a sinc pulse of bandwidth 3kHz centred at 2kHz

137 from the water peak, between the fat and silicone resonances, to suppress
138 both fat and silicone.

139 2.5. Software Co-registration

140 The main objective of any general co-registration software is to merge
141 the coordinate system of the moving image I_M with the fixed (or reference)
142 image I_F . The transformation matrix T is used to warp the moving image
143 in order to minimise the error metric with the fixed image. This process is
144 iterated until a certain convergence criterion is reached.

145 A landmark-based co-registration approach [16] based on non-reflective
146 similarity with the addition of optional reflection was used to register the
147 tumour areas between modalities, utilising a set of prominent anatomical
148 features including the tumour edges and spine location as landmarks. The
149 positions of these features, identified manually, were denoted in the MR image
150 as I_M , and the matching positions in the MSOT image as I_F . These vectors
151 were then used to calculate the transformation matrix and transform both
152 modalities into the same coordinate space, minimising the euclidean distance
153 between the landmarks.

154 The registration procedure was implemented in two steps. The first step
155 ensured proper alignment between the body contours in MSOT and MRI,
156 while the second step provided further alignment of the tumours. Landmarks
157 for the first step were the spine and characteristic anatomical features visible in
158 MRI and MSOT, such as contact points between tumors and body (Figure 3).
159 Second step landmarks were defined by points along the outline of the tumour:
160 up to two points on an axis between the tumour and mouse body; and up to
161 two points on the perpendicular axis (Figure 5). The corresponding similarity-
162 based transformation matrix was calculated using the MATLAB function
163 *fitgeotrans*.

164 2.6. Image and Statistical Analysis

165 All image analysis was performed in MATLAB 2016a (Mathworks) using
166 the Image Processing Toolbox, the Computer Vision Toolbox and custom
167 scripts unless otherwise stated. All image data and custom analysis codes
168 will be made openly available at doi: 10.17863/CAM.39741.

169 Image reconstruction was performed using an acoustic backprojection
170 algorithm (iThera Medical GmbH) with an electrical impulse response cor-
171 rection, to account for the frequency dependent sensitivity profile of the
172 transducers. Images were reconstructed with a pixel size of $100\ \mu\text{m} \times 100\ \mu\text{m}$

173 which is approximately equal to half of the in-plane resolution of the InVision
174 256-TF. Pseudoinverse matrix inversion (pinv function in MATLAB 2016a)
175 was applied to the measured optoacoustic spectrum in each pixel to calculate
176 the relative oxy- [HbO_2] and deoxy-haemoglobin [Hb] signal. The presented
177 images illustrate the total haemoglobin signal [$HbO_2 + Hb$] unless otherwise
178 stated. Apparent blood oxygen saturation SO_2^{MSOT} was calculated as a ratio
179 of oxy- to total haemoglobin [4].

180 All MR images were flipped horizontally prior to image registration. The
181 position of the slice analysed was chosen by the operator to best match the
182 location of the imaging slice in OT, acquired directly before the MRI.

183 The analysis of registration accuracy of body and tumour contours was
184 performed by calculating the Dice Similarity Coefficient (DSC). This coefficient
185 is defined as:

$$DSC = \frac{2|X \cap Y|}{|X| + |Y|}$$

186 , which allows quantification of the overlap between two binary masks, X
187 and Y (i.e. original MRI body/tumour mask and the mask obtained from
188 the MSOT image after co-registration). The higher the DSC, the better the
189 overlap between the two binary masks and therefore, the more accurate the
190 image registration result.

191 The results were compared on a per-tumour basis. Differences in DSCs
192 between conventional and novel holder geometries as well as before and after
193 landmark-based registrations (for body and tumor) were statistically tested
194 with two-tailed paired t-tests (in the case of equal variances between sets of
195 samples) and two-tailed unpaired t-tests (in the case of unequal variances
196 between sets of samples). Data are reported as median \pm standard deviation,
197 unless otherwise stated.

198 DCE-MRI signal Area under the Curve (AuC) 1 minute after contrast
199 administration was compared to the change in blood oxygen saturation
200 (SO_2^{MSOT}) as measured by Oxygen Enhanced Optoacoustic Tomography in
201 response to an oxygen challenge [4]. The median DCE AuC values in the
202 regions showing positive SO_2^{MSOT} response and the rest of the tumour area
203 were compared, with the pixels classified as positively responding when the
204 difference between the average SO_2^{MSOT} in the first 20 frames (under air
205 breathing) and the the last 20 frames (oxygen breathing), exceeded twice the
206 standard deviation of the SO_2^{MSOT} in the first 20 frames.

3. Results

3.1. Novel holder geometry improves visual anatomical similarity between MSOT and MRI

Visual inspection of MRI and MSOT images acquired with the conventional and novel MRI holder geometries yielded distinct differences in body shape and anatomical appearance (Figure 3). Overall body shape and relative tumour location were not easily comparable for tumours imaged with the conventional protocol, while the novel protocol showed a high degree of similarity in body contour and tumour locations. A quantitative comparison of the contours of the mouse bodies in MSOT and MRI images using Dice similarity coefficients (DSCs) showed significant improvement ($p=0.03$, unpaired t-test) with the novel MRI holder, resulting in a higher DSC (0.63 ± 0.05 vs. 0.52 ± 0.07 , novel vs. conventional). The higher DSC indicates that the novel MRI holder more accurately represents the body deformation observed in the MSOT.

3.2. Landmark-based contour registration improves animal body alignment

Landmark-based contour registration was then applied to MSOT and MR images acquired using both the conventional and novel MRI holders (illustrated in Figure 4a). The difference between the conventional and novel MRI holders was more significant ($p=0.002$, unpaired t-test) following landmark-based registration with further improved DSCs (0.92 ± 0.02 vs. 0.83 ± 0.03 , novel vs. conventional). In total (Figure 4b), the contour registration procedure improved DSCs for body contour overlay significantly, both for the conventional ($\Delta\text{DSC} = 0.31$, $p=0.004$, paired t-test) and novel ($\Delta\text{DSC} = 0.29$, $p=7.2 \times 10^{-5}$, paired t-test) holder.

3.3. Landmark-based tumour contour optimisation further improves local anatomical similarity

Following the body contour registration, each tumour was individually co-registered as an additional optimisation step. The tumour contours showed a qualitatively higher agreement after this additional landmark-based optimisation. The gain in registration accuracy was estimated to be between 5 and 15 pixels ($375 \mu\text{m} - 1125 \mu\text{m}$), based on the distances between the co-registered tumour outlines (Figure 5a). Quantitative assessment resulted in a significant improvement in tumour mask overlay DSCs ($p=0.005$, paired t-test) after landmark-based transformation of tumour masks (pre-transform: 0.85 ± 0.06 vs. post-transform: 0.92 ± 0.04 , Figure 5b).

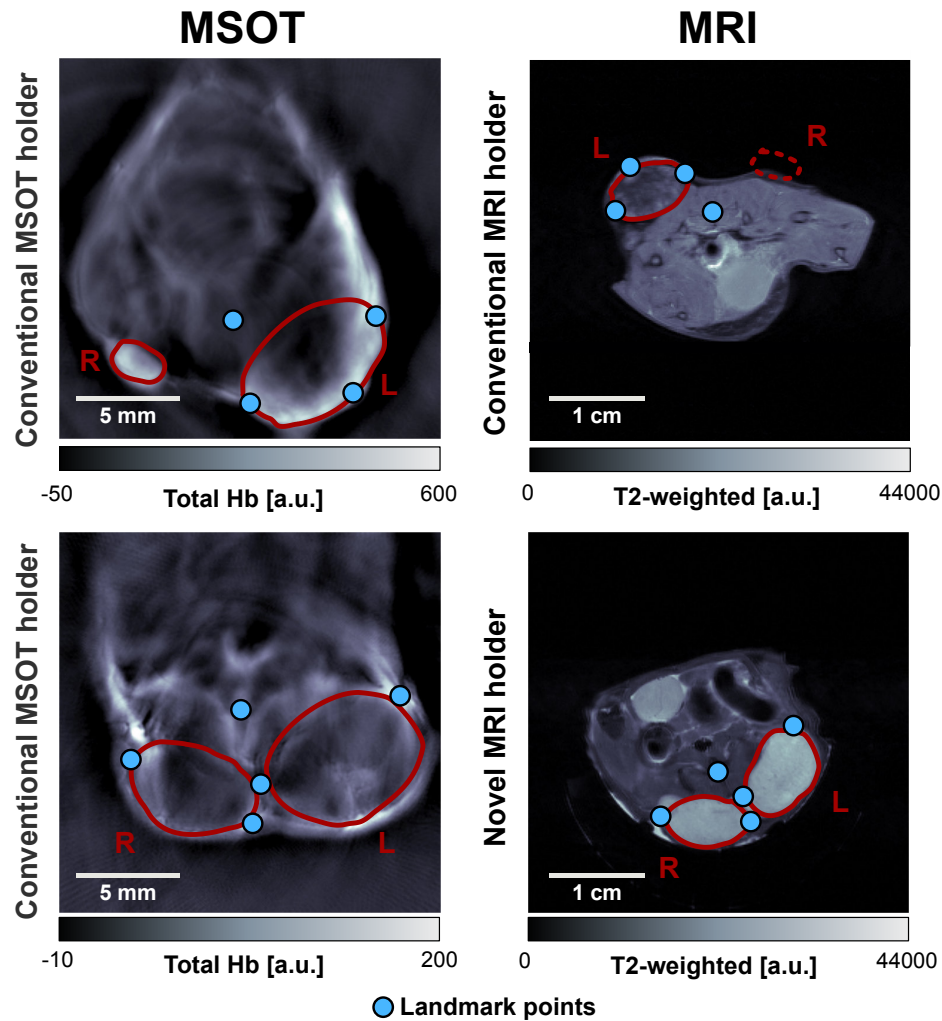


Figure 3: **Qualitative comparison of tomographic image data from OT and MRI modalities using the conventional and novel MRI holders.** *Top:* MSOT/MRI image pair with conventional holder geometry as in Figure 1. Tumour R is not visible in the corresponding MR image. *Bottom:* MSOT/MRI image pair with novel holder geometry as in Figure 2.

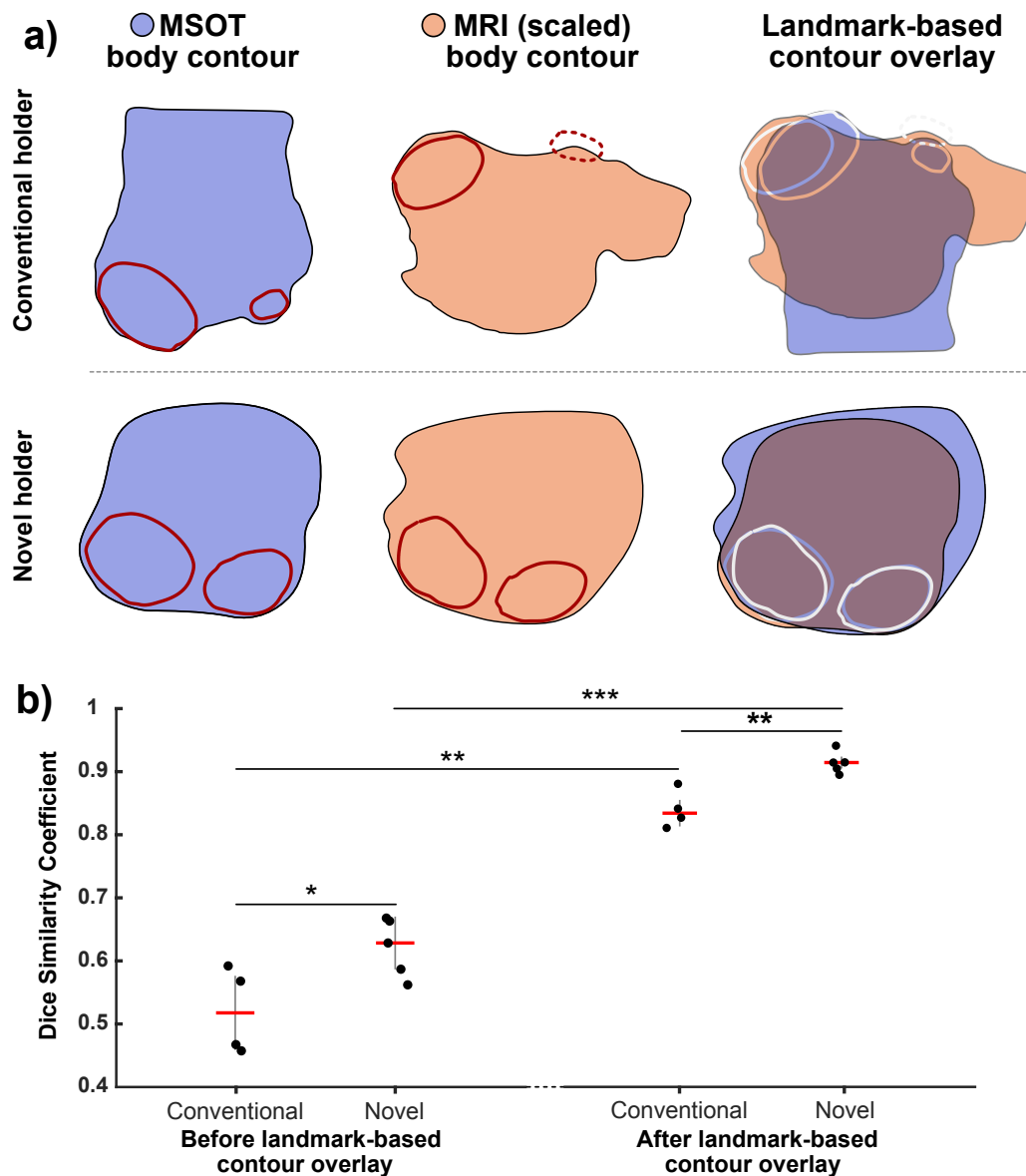


Figure 4: **Comparison of body contour overlays of MRI/MSOT image pairs for conventional and novel holder geometries.** (a) Body contour pairs (derived from binarized body outlines) for MSOT and MRI. Use of the novel protocol improves the agreement substantially (overlaid MSOT and MRI contours shown in blue and orange respectively). (b) Quantitative comparison of Dice similarity coefficient ($n=4$ for conventional holder and $n=5$ for novel MRI holder). * $p<0.05$, ** $p<0.01$, *** $p<0.001$ by unpaired two-tailed t-test (unequal variances) and paired two-tailed t-test (equal variances).

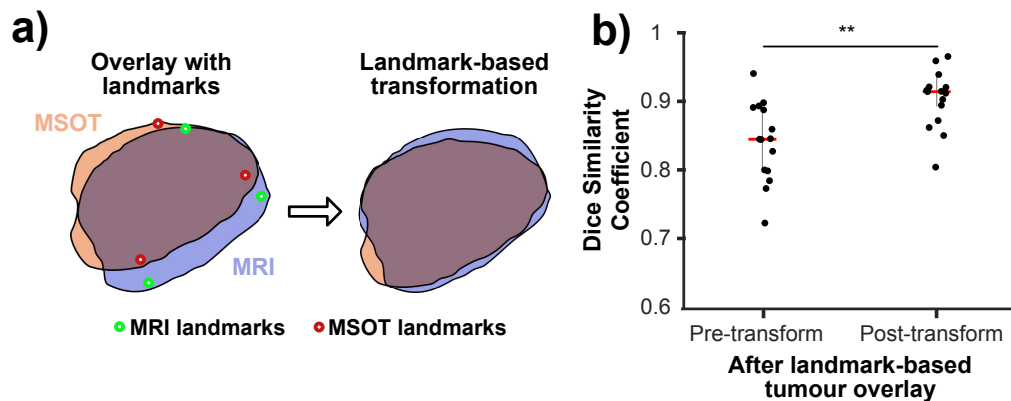


Figure 5: **Overlays of tumour contours from MRI/MSOT image pairs before and after landmark-based optimization.** (a) Comparison of a tumour outline before and after landmark-based tumour registration. (b) Quantification of the improvement in Dice similarity coefficient (n=15 tumours, combined data for conventional and novel MRI holder geometry). ** p<0.01 by paired two-tailed t-test (equal variances).

3.4. Application of the co-registration framework for comparison of data acquired using MSOT and MRI

Comparison of the anatomical similarity of the imaging data from the two modalities subjected to our co-registration framework was made in three K8484 tumour bearing mice. K8484 tumours were used for this purpose as they contain heterogeneous structural features visible in both MSOT and MRI. Upon visual inspection of images from three mice bearing this tumour type, it can be seen that the body shapes and tumour locations images demonstrate high anatomical similarity (Figure 6). Considering the feature locations (defined as distinct features in MRI and MSOT images belonging to the same structure, denoted by red annotations in Figure 6), we established that the relative distance between the centres of the features between modalities showed a close agreement (2,4, and 12 pixels, or 150, 300 and 900 μm respectively for the three mice shown). In Figure 6, the red rectangle indicates the extent of the observed features in MRI/MSOT image pairs, whereas the red asterisk highlights the most distinct point within the feature. This point was subsequently used for determining the relative distance between modalities.

A comparison of functional imaging data was then made in these K8484 tumours based on imaging data recorded using DCE-MRI and Oxygen Enhanced OT (OE-OT) protocols, which have been previously shown to relate

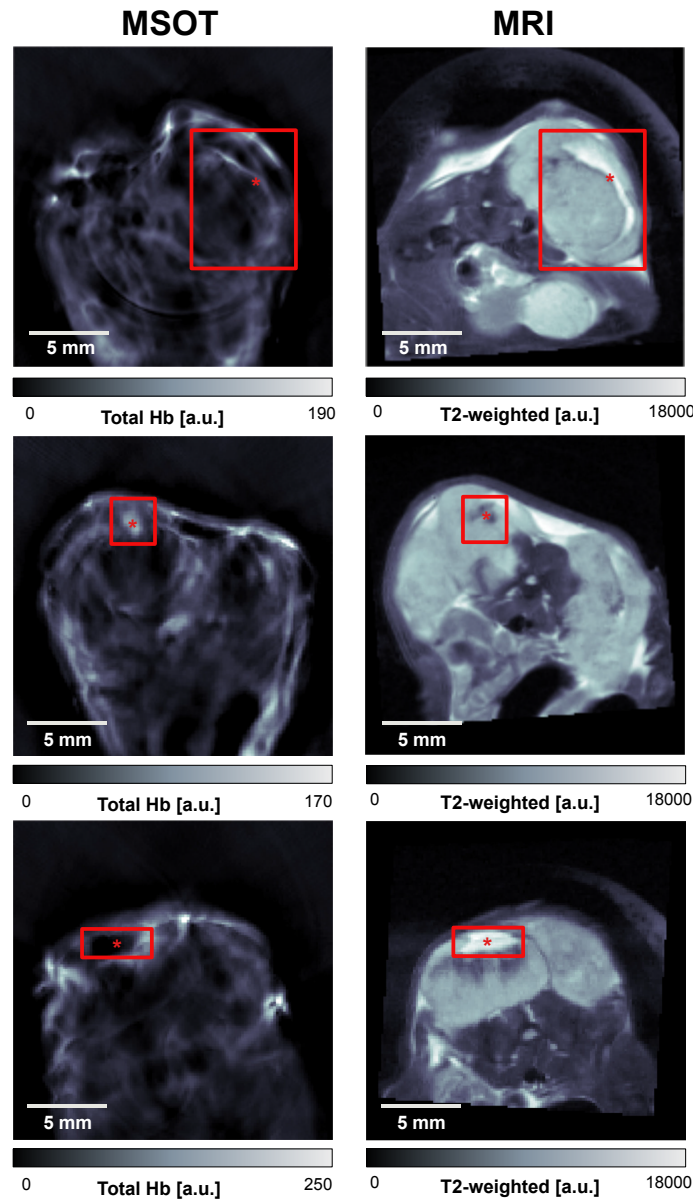


Figure 6: **Anatomical features in three K8484 tumours after landmark-based body and tumour contour registration.** All tumours contained distinct intratumoural features (highlighted in red). The distances between the estimated feature centroids (marked with red asterisks) were measured to be very small after registration, with a range from 2 to 12 pixels (150 μ m to 900 μ m).

to tumour perfusion and vascular function [6]. Visual comparison of DCE-MRI and OE-OT images (Figure 7a) shows a similar distribution of perfused pixels in both modalities, with a greater number in the rim compared to the core of the tumour, as is commonly reported in subcutaneous xenografts. Quantitative comparison of DCE-MRI enhancement in regions of OE-OT response (Figure 7b) shows a markedly stronger DCE-MRI enhancement in the areas showing positive response in the OE-OT, suggesting a functional relationship between these imaging biomarkers.

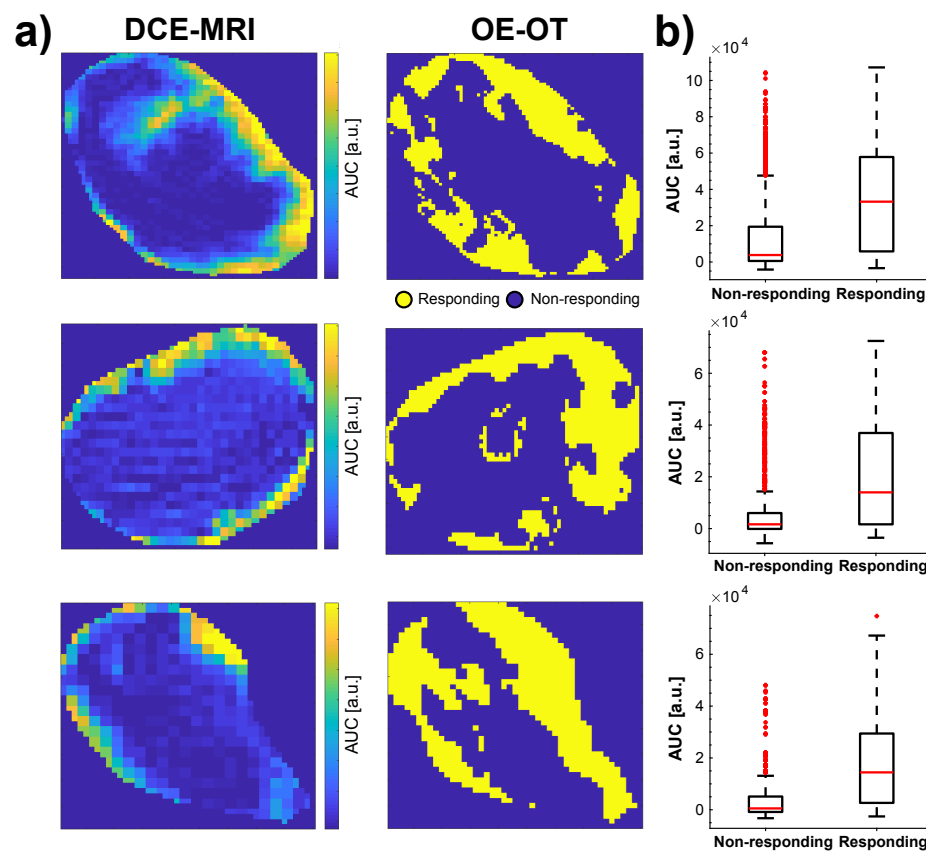


Figure 7: Measurements of vascular function show strong co-localisation in MRI and MSOT. (a) Maps of DCE-MRI area under the curve (AUC) enhancement 1 minute after contrast injection (left) are in close spatial agreement with the maps of positive response to oxygen challenge in Oxygen-Enhanced Optoacoustic Tomography (right). (b) The DCE-MRI AUC is clearly higher in the areas positively responding in OE-OT.

271 4. Discussion

272 Co-registration of images between modalities enables the combination of
273 complementary information provided by different imaging methods. Due to
274 deformation of the animal or patient between scans, correct alignment of
275 images can pose a significant challenge and require both hardware and software-
276 based optimisation approaches. In this work, we describe an integrated
277 hardware and software framework for co-registration of small animal MSOT
278 and MR imaging data. Without co-registration, these modalities produce
279 very different images of the sample, due to different animal positioning and
280 stress distribution.

281 On the hardware side, a novel silicone MRI animal holder was developed,
282 which was designed to mimic the external stresses acting on the mouse body
283 in the MSOT. Introducing the new holder alone already significantly improved
284 the similarity in the shape of the entire mouse body contour as well as the
285 individual tumour contour, contributing to more accurate co-registration.
286 Importantly, the use of the holder did not increase animal preparation time
287 or cause any side effects for animal welfare during imaging. Fabrication of
288 the holder is simple and inexpensive, as soft two-component silicone is poured
289 over a 3D printed mouse mold. The protocol offers a simple solution to
290 improve MSOT/MR image co-registration.

291 A software tool for landmark-based image co-registration was then estab-
292 lished to further improve the co-registration and enable per-pixel analysis
293 of the combined multi-modal images. The transformation matrix for the
294 MSOT images was calculated to maximise similarity between body and
295 tumour outlines in both modalities as well as to minimise the distances
296 between anatomical landmarks. The result of applying this software tool
297 was a co-localisation error in the order of 100 microns, comparable to the
298 typical resolution of both modalities. This framework also enabled per-pixel
299 combination and comparison of the insight offered by MSOT and MRI in
300 functional imaging. The relationship between tumour perfusion, provided by
301 early DCE-MRI enhancement [9], and vascular function, given by the MSOT
302 response to oxygen challenge [6], served as a proof of concept for further
303 MSOT/MRI comparison.

304 Despite the clear improvements in image co-registration achieved, there
305 remain some limitations to our study. Firstly, the described two-step hardware
306 and software framework is designed to aid with 2D co-registration, which
307 assumes already the correct, manual choice of matching imaging slice between

the modalities. The use of the silicone holder can help in this task to some extent, as the similar cross-sectional shape of the tumour in the MRI can help match it qualitatively to the geometry in the MSOT. Slice misalignment will introduce additional error in the co-registration procedure.

A second limitation arises in the design of the silicone bed, which aimed to mimic the effects of the polyethylene film holder used in the MSOT, as well as the stresses due to water submersion during MSOT imaging. In order to support the weight of the animal, the silicone had to be stiffer than optimal, causing some discrepancy in MRI/MSOT mouse positioning. Further optimisation using silicones of different elastic properties could better match the distribution of forces and should be investigated in future experiments.

Finally, the silicone bed was created for a specific mouse size based on the typical usage in our experiments. If needed, additional silicone beds could be created to account for different mouse sizes, across strain and age for instance, and taking the individual tumour position into consideration. The optimal approach would utilize 3D modeling to create mouse-specific holders and require standardisation of the modelling, printing and casting workflow.

4.1. Conclusion

We have demonstrated the feasibility of a hardware- and software-based image registration framework for MRI and MSOT images. We use a novel silicone MRI holder, as well as a software tool to perform landmark-based co-registration of the images. Both steps led to a significant improvement in the registration of the tumour outlines and internal structure between the modalities. This simple, inexpensive approach can be readily implemented for multi-modal MSOT/MRI studies of small animals, which will help to provide valuable insight into relative performance of these two modalities in revealing vascular architecture and function in cancer.

5. Acknowledgements

This work was supported by Cancer Research UK (C47594/A16267, C14303/A17197) and the EPSRC-CRUK Cancer Imaging Centre in Cambridge and Manchester (C197/A16465 and C8742/A18097). We would like to thank the CRUK CI Core Facilities for their support of this work, in particular the Imaging Core, Biological Resource Unit, Histopathology, and Biorepository. We also want to thank Mireia Crispin-Ortuzar and Joanna Brunker for helpful comments on the draft article.

- 343 [1] V. Ntziachristos, D. Razansky, Molecular imaging by means of multi-
344 spectral optoacoustic tomography (msot), *Chemical reviews* 110 (2010)
345 2783–2794.
- 346 [2] M. Li, Y. Tang, J. Yao, Photoacoustic tomography of blood oxygenation:
347 A mini review, *Photoacoustics* 10 (2018) 65–73.
- 348 [3] J. Laufer, P. Johnson, E. Zhang, B. Treeby, B. Cox, B. Pedley, P. Beard,
349 In vivo preclinical photoacoustic imaging of tumor vasculature develop-
350 ment and therapy., *Journal of Biomedical Optics* 17 (2012) 056016.
- 351 [4] M. R. Tomaszewski, I. Q. Gonzalez, J. P. O'Connor, O. Abeyakoon,
352 G. J. Parker, K. J. Williams, F. J. Gilbert, S. E. Bohndiek, Oxygen En-
353 hanced Optoacoustic Tomography (OE-OT) Reveals Vascular Dynamics
354 in Murine Models of Prostate Cancer, *Theranostics* 7 (2017) 2900–2913.
- 355 [5] S. E. Bohndiek, L. S. Sasportas, S. Machtaler, J. V. Jokerst, S. Hori,
356 S. S. Gambhir, Photoacoustic Tomography Detects Early Vessel Re-
357 gression and Normalization During Ovarian Tumor Response to the
358 Antiangiogenic Therapy Trebananib., *Journal of nuclear medicine : official publication, Society of Nuclear Medicine* 56 (2015) 1942–7.
- 360 [6] M. R. Tomaszewski, M. Gehrung, J. Joseph, I. Quiros-Gonzalez, J. A.
361 Disselhorst, S. E. Bohndiek, Oxygen-Enhanced and Dynamic Contrast-
362 Enhanced Optoacoustic Tomography Provide Surrogate Biomarkers of
363 Tumor Vascular Function, Hypoxia, and Necrosis., *Cancer Research* 78
364 (2018) 5980–5991.
- 365 [7] R. A. Little, H. Barjat, J. I. Hare, M. Jenner, Y. Watson, S. Cheung,
366 K. Holliday, W. Zhang, J. P. O'Connor, S. T. Barry, S. Puri, G. J.
367 Parker, J. C. Waterton, Evaluation of dynamic contrast-enhanced MRI
368 biomarkers for stratified cancer medicine: How do permeability and
369 perfusion vary between human tumours?, *Magnetic Resonance Imaging*
370 46 (2018) 98–105.
- 371 [8] R. R. Hallac, H. Zhou, R. Pidikiti, K. Song, S. Stojadinovic, D. Zhao,
372 T. Solberg, P. Peschke, R. P. Mason, Correlations of noninvasive BOLD
373 and TOLD MRI with pO₂ and relevance to tumor radiation response,
374 *Magnetic Resonance in Medicine* 71 (2014) 1863–1873.

- 375 [9] J. P. B. O'Connor, J. K. Boulton, Y. Jamin, M. Babur, K. G. Finegan, K. J.
376 Williams, R. A. Little, A. Jackson, G. J. M. Parker, A. R. Reynolds,
377 J. C. Waterton, S. P. Robinson, Oxygen enhanced MRI accurately
378 identifies, quantifies, and maps hypoxia in preclinical cancer models.,
379 Cancer Research (2015) 5472.
- 380 [10] M. Grade, J. A. Hernandez Tamames, F. B. Pizzini, E. Achten, X. Golay,
381 M. Smits, A neuroradiologist's guide to arterial spin labeling MRI in
382 clinical practice., Neuroradiology 57 (2015) 1181–202.
- 383 [11] M. Weigert, U. Pietrzyk, S. Müller, C. Palm, T. Beyer, Whole-
384 body PET/CT imaging: combining software- and hardware-based co-
385 registration., Zeitschrift für Medizinische Physik 18 (2008) 59–66.
- 386 [12] H. F. Wehrl, A. W. Sauter, M. R. Divine, B. J. Pichler, Combined
387 PET/MR: A Technology Becomes Mature, Journal of Nuclear Medicine
388 56 (2015) 165–168.
- 389 [13] A. B. E. Attia, C. J. H. Ho, P. Chandrasekharan, G. Balasundaram,
390 H. C. Tay, N. C. Burton, K.-H. Chuang, V. Ntziachristos, M. Olivo,
391 Multispectral optoacoustic and MRI coregistration for molecular imaging
392 of orthotopic model of human glioblastoma, Journal of Biophotonics 9
393 (2016) 701–708.
- 394 [14] W. Ren, H. Skulason, F. Schlegel, M. Rudin, J. Klohs, R. Ni, Automated
395 registration of magnetic resonance imaging and optoacoustic tomography
396 data for experimental studies, Neurophotonics 6 (2019) 1.
- 397 [15] J. Joseph, M. R. Tomaszewski, I. Quiros-Gonzalez, J. Weber, J. Brunner,
398 S. E. Bohndiek, Evaluation of Precision in Optoacoustic Tomography
399 for Preclinical Imaging in Living Subjects., Journal of Nuclear Medicine
400 58 (2017) 807–814.
- 401 [16] J. Modersitzki, FAIR: flexible algorithms for image registration, volume 6,
402 Society for Industrial and Applied Mathematics, 2009.